Generation and propagation of internal tides and solitary waves at the shelf edge of the Bay of Biscay

Xu Hu Xie, Yannis Cuypers, Pascale Bouruet-Aubertot, Annick Pichon, Antonio Lourenço, Bruno Ferron

AGU PUBLICATIONS

JGR

Journal of Geophysical Research: Oceans

RESEARCH ARTICLE

10.1002/2015JC010827

Generation and propagation of internal tides and solitary waves at the shelf edge of the Bay of Biscay

X. H. Xie[1,2], Y. Cuypers[2], P. Bouruet-Aubertot[2], A. Pichon[3], A. Lourenço[1], and B. Ferron[4]

[1]State Key Laboratory of Tropical Oceanography, South China Sea Institute of Oceanology, Chinese Academy of Sciences, Guangzhou, China, [2]LOCEAN, UMR7167, Université Pierre et Marie Curie, Paris, France, [3]SHOM, Centre Militaire d'Océanographie, Brest, France, [4]LPO, Ifremer, UMR 6523 CNRS-IFREMER-IRD-UBO, Brest, France

Key Points:
- Onshore and offshore traveling internal tides and solitary waves are observed
- Numerical models reproduce observed internal tides and solitary waves
- Advection affects generation and propagation of internal tide and solitary wave

Correspondence to:
X. Xie,
xhxie@scsio.ac.cn

Citation:
Xie, X. H., Y. Cuypers, P. Bouruet-Aubertot, A. Pichon, A. Lourenço, and B. Ferron (2015), Generation and propagation of internal tides and solitary waves at the shelf edge of the Bay of Biscay, *J. Geophys. Res. Oceans*, *120*, 6603–6621, doi:10.1002/2015JC010827.

Received 9 MAR 2015
Accepted 3 SEP 2015
Accepted article online 7 SEP 2015
Published online 3 OCT 2015

Abstract High-frequency mooring data were collected near the northern shelf edge of the Bay of Biscay to investigate the generation and propagation of internal tides and internal solitary waves (ISWs). During spring tide, strong nonlinear internal tides and large amplitude ISWs are observed every semidiurnal tidal period. While onshore propagation was expected since the mooring is located shoreward of the maximum internal tidal generation location, both onshore and seaward traveling internal tides are identified. Within a tidal period at spring tide, three ISW packets are observed. Like internal tides, different ISW packets have opposite (seaward and shoreward) propagating direction. Based on realistic hydrostatic HYCOM simulations, it is suggested that advection by the barotropic tide affects wave generation and propagation significantly and is essential for the seaward traveling internal tides to appear shoreward of their generation location. A two-layer idealized nonhydrostatic model derived by Gerkema (1996) further confirms the effect of advection on the generation and propagation of internal tides. Moreover, the two-layer model reproduces one seaward propagating ISW packet and one shoreward propagating ISW packet, indicating that the offshore and onshore traveling ISWs are excited by nonlinear steepening of the seaward and shoreward traveling internal tides, respectively.

1. Introduction

Internal tides (internal waves with tidal frequency) are frequently observed over continental shelf and slope regions around the world. Their dissipation may play an important role in the global oceanic energy budget and local mixing [*St. Laurent and Garrett*, 2002; *Garrett and Kunze*, 2007]. Internal tides over the continental shelf and slope are mainly generated via an interaction between the barotropic tide and the steep shelf break, after which they propagate both onshore and offshore [e.g., *Gerkema and Zimmerman*, 1995]. In many cases, steepening of the shoreward-propagating waves is associated with the generation of large amplitude nonlinear internal solitary waves (ISWs) over continent shelves [e.g., *Holloway et al*., 1997; *Ramp et al*., 2004; *Scotti et al*., 2007].

The northern continental slope of the Bay of Biscay is well known for its large barotropic to baroclinic tide conversion rate [*Baines*, 1982; *Gerkema et al*., 2004; *Pichon and Correard*, 2006, *Pichon et al*., 2013]. Many numerical models and observations have shown that internal tides observed near this slope are generated close to the 200 m isobath [e.g., *Baines*, 1982; *Pingree et al*., 1986; *Lam et al*., 2004]. Once generated, the seaward traveling internal tides have a beam-like structure [*Pingree and New*, 1989, 1991], while the shoreward traveling internal tides can be described in terms of few vertical modes [*Pingree et al*., 1986; *Pichon and Mazé*, 1990]. Furthermore, the internal tides over the continental edge are often characterized by strong nonlinearities [*Mazé*, 1987; *Pichon and Mazé*, 1990]. Observations from cruises and satellite imagery have also shown the occurrence of large amplitude ISWs with short period and wavelength [e.g., *Pingree and Mardell*, 1985; *New and Da Silva*, 2002; *Xie et al*., 2013]. Since these waves often appear in troughs of internal tides, they are conjectured to result from the nonlinear steepening of internal tides [*Pingree et al*., 1986; *New and Pingree*, 2000]. However, satellite imagery shows the complexity and 3-D nature of ISWs near the shelf break of the northern Bay of Biscay: there are ISW packets with multiple propagation directions that are possible for ISW generation at different source locations along the shelf break [*New*, 1988; *New and Da Silva*, 2002]. Until now, long-term observations of these high-frequency waves providing detailed information on their generation process and phasing with the internal tide are still lacking.

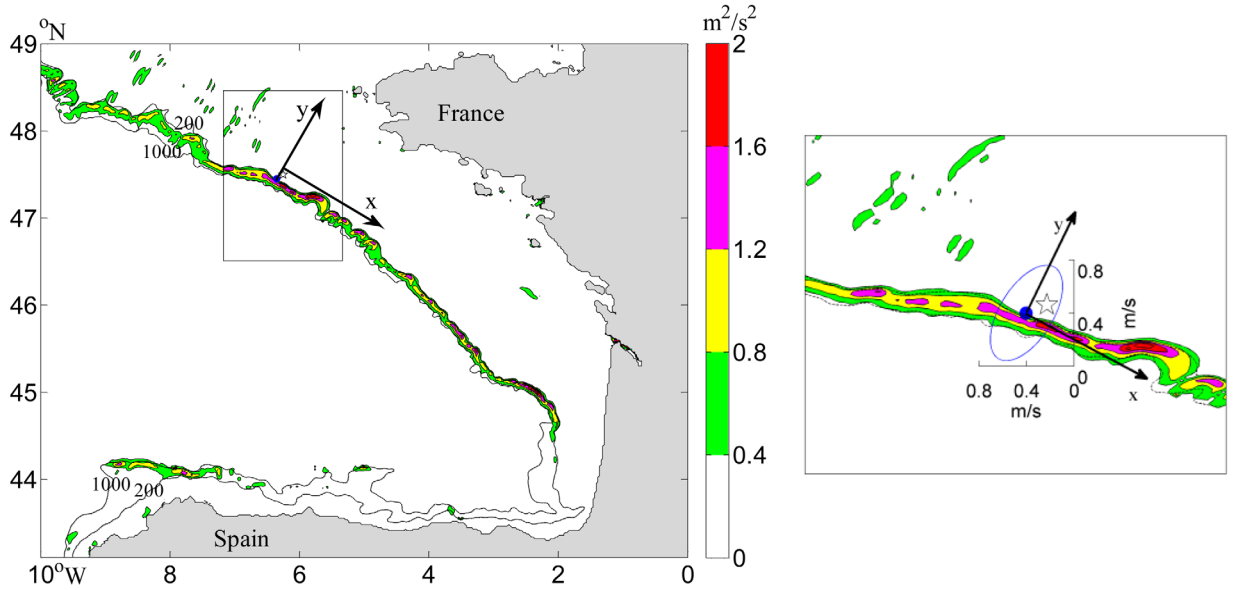

Figure 1. Map showing bathymetry, mooring site (blue point), and CTD/LADCP station (star) in the Bay of Biscay. *x* and *y* axes indicate the along-shore and cross-shore direction, respectively. Colors represent the vertical integration from 0 to *H* of the forcing term *F*(*z*). The left plot is for the whole Bay of Biscay, while the right plot is for the area indicated by the rectangle in the left plot. Barotropic M_2 tidal current ellipse at mooring site is shown in the right plot.

In this paper, a 14 day long mooring data set with high time-sampling rate (<1 min) collected at the Armorican shelf edge in the northern Bay of Biscay is used to investigate the generation and propagation of internal tides and ISWs. Output from a 3-D hydrostatic numerical model, HYCOM, which reproduces the observed nonlinear internal tides, provides further insight on the internal tide generation and propagation. In addition to HYCOM model, a two-layer nonhydrostatic model is also implemented to explore the generation process of ISWs.

In section 2, the methodology is described. We next present an overview of the observations in section 3. In section 4, the HYCOM model is used to investigate the generation and propagation of internal tides. General properties and generation mechanism of the observed high-frequency nonlinear internal waves are characterized using an idealized nonhydrostatic model in section 5. Summary and discussion are given in section 6.

2. Methodology

2.1. Mooring Data

Data were collected during the French Service Hydrographique et Océanographique de la Marine (SHOM) experiment in summer 2008. A mooring equipped with current meters and high-frequency temperature sensors was deployed at the shelf edge (47.44°N, 6.36°W), where the water depth *H* is ∼174 m (Figure 1). The mooring consisted of a Seaguard (at 20 m depth) and three Aquadopp (at 65, 115, and 164 m depths) current meters, 10 RBR temperature/pressure sensors (at 27, 42, 57, 72, 87, 102, 117, 132, 147, and 166 m) and two SBE37 conductivity/temperature/pressure sensors (at 90 and 162 m depths). Seaguard and Aquadopp current meters sampled at 30 and 300 s intervals, respectively, while the time sampling of RBR and SBE37 was of 5 and 30 s, respectively. The observation period was scheduled from 29 August to 22 September, 2008. However, we only obtained an effective observation record of approximately 14 days (from 29 August to 13 September) due to unexpected recovery by a fishing boat. Data from current meter at 65 m and RBR at 147 m are not used due to a shorter effective record. Depth positions of the sensors used in this paper are plotted in Figure 2.

With this 14 day mooring observation record, the spring-neap tidal modulation can be clearly identified in the time series of the measured velocity field (Figure 3). During spring tide, combined CTD/LADCP yo-yoing was performed at a fixed site (47.50°N, 6.25°W; *H* =165 m) ∼10 km away from the mooring site (marked by

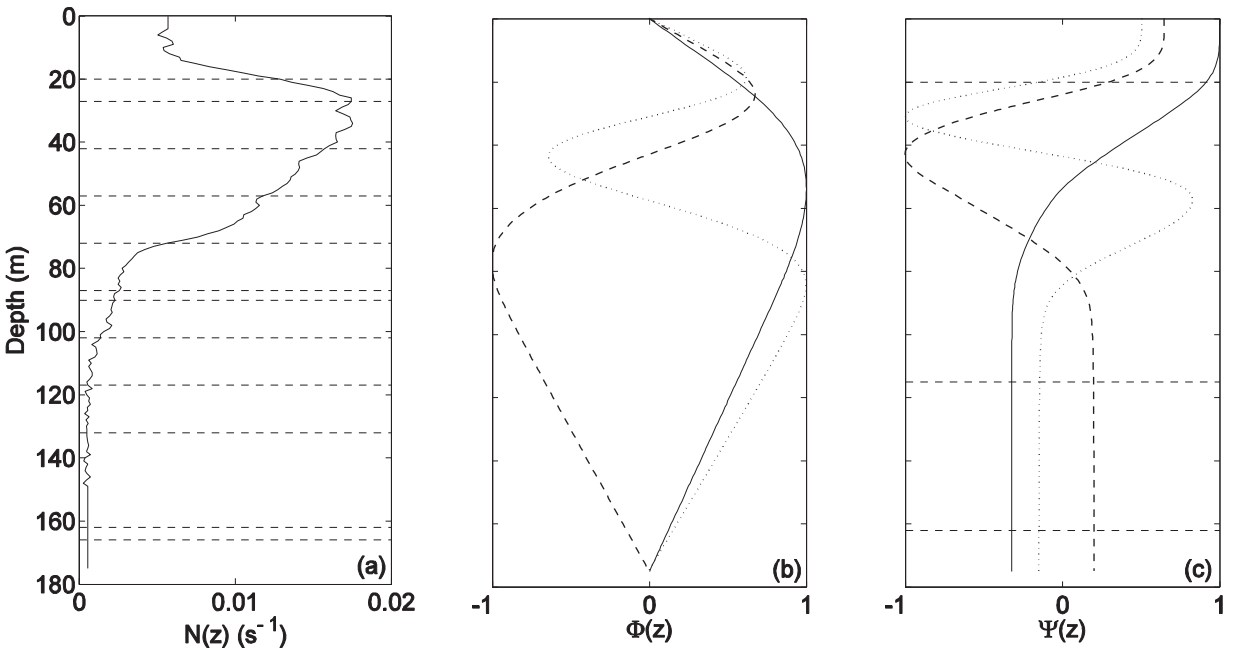

Figure 2. The profiles of buoyancy frequency (a) computed from CTD data and modal functions of (b) vertical displacement and (c) horizontal velocity for first three baroclinic modes. Horizontal dashed lines in Figures 2a and 2c indicate locations of temperature sensors and current meters used in this study, respectively.

a star in Figure 1). The measurements started at 13:30 on 29 August and continued until 17:50 the next day. During this measurement period of ~28 h, 155 casts were made. The effective depth range is from 4 to 150 m, covering ~88% of the water column. These fixed point CTD data are used to compute the mean depth of isopycnals over the first 25 h (two tidal cycles) and the background stratification $N(z)$ at the mooring site. Since measurements do not cover the full water column, $N(z)$ near the bottom is absent. At these

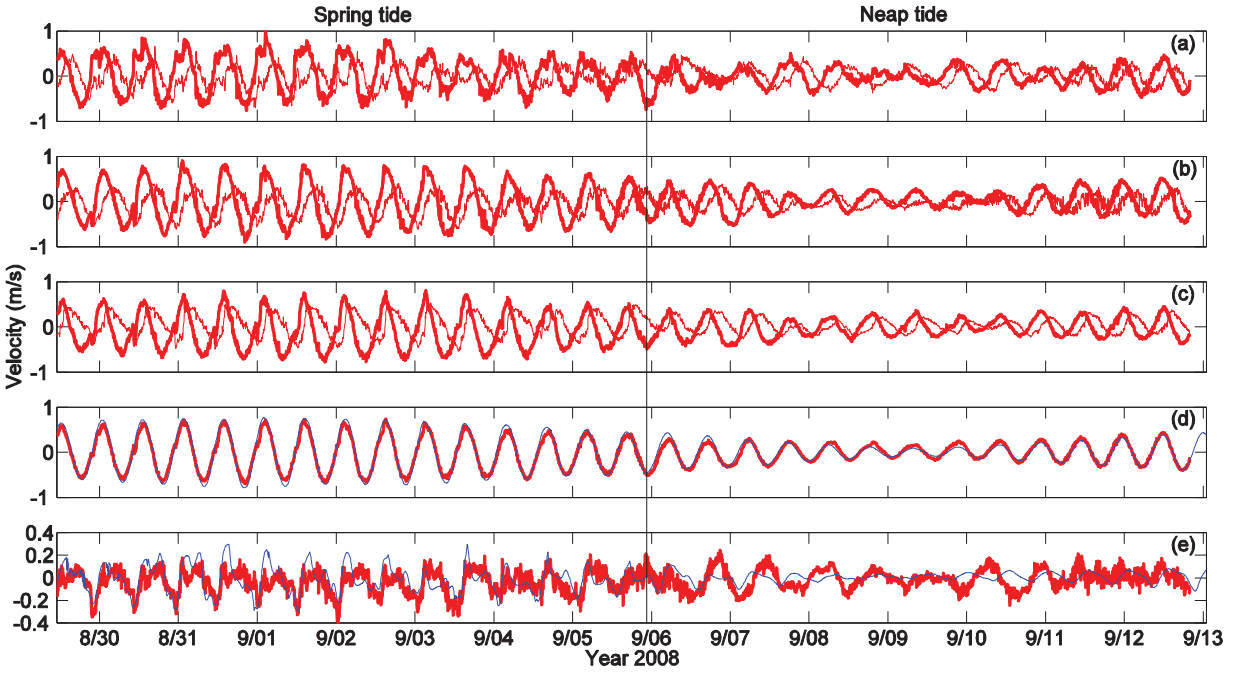

Figure 3. Time series of currents observed at depths of (a) 20, (b) 115, and (c) 164 m. The thick and thin lines represent the cross-shore and along-shore velocities, respectively. (d) The cross-shore barotropic current velocity and (e) baroclinic velocity at a depth of 115 m obtained from observation (red) and HYCOM model (blue). The vertical line indicates the boundary between spring and neap tides.

depths, $N(z)$ is assumed to be equal to that at the nearest effective depth. Based on $N(z)$ with a complete depth profile (Figure 2a), modal functions of vertical displacement and horizontal velocity, $\Phi_n(z)$ and $\psi_n(z)$ (n is the mode number), are calculated [*Gill*, 1982] (Figures 2b and 2c).

2.2. Numerical Model

2.2.1. HYCOM Model

The hybrid coordinate ocean model HYCOM [*Bleck*, 2002] is used to simulate internal tidal waves in the Bay of Biscay. The model domain covers the entire Bay of Biscay from 43°N to 51°N and from 15°W to the French Coast, with a horizontal resolution of 2 kilometers (km). In the model, isopycnal coordinates are used in an adiabatic mode, without diffusion of density, temperature, and salinity. By using a time average of CTD stations collected during the experiment, a vertical stratification is defined by 32 isopycnal layers. In the upper 100 m, the layer thickness is 10 m, while it varies from 50 to 150 m below 100 m. A viscosity coefficient is introduced in the momentum equations as $\nabla\bullet[\nu\nabla\bullet u]$ to define turbulent and numerical diffusions: ν_{turb} and ν_{num}, where $\nu=\max(\nu_{num},\nu_{turb})$. These two viscosity coefficients are computed by

$$\nu_{turb}=\lambda\left[\left(\frac{\partial u}{\partial x}-\frac{\partial v}{\partial y}\right)^2+\left(\frac{\partial u}{\partial x}+\frac{\partial v}{\partial y}\right)^2\right]^{1/2}dX^2 \tag{1}$$

and $\nu_{num}=veldff.dX$, where dX is the horizontal resolution of HYCOM model, $veldff=0.0075$ m s^{-1} and $\lambda=0.2$. Since ν_{turb} varies with the deformation of the velocity field (equation (1)), the horizontal viscosity varies from 15 to 120 m^2 s^{-1}. The model is forced at the boundaries with the four main semidiurnal components M_2, S_2, N_2, and K_2 and there is no atmospheric forcing (wind stress and air-sea fluxes). The initial density field is homogeneous in the horizontal plane. The initial condition of the velocity field is defined by the barotropic tide. The baroclinic part of the tidal current is relaxed to zero at the open boundaries by using a sponge layer. Other detailed description of the model configuration can be found in *Pichon et al*. [2013] (see the configuration SCHEM-HYCOM in section 2.2 of their paper).

The model run starts on 15 August 2008 until 15 September 2008, thus covering the observation period. Temperature and velocity outputs are then interpolated vertically onto a 2 m grid. To quantify the internal tide generation, model data are used to compute the forcing term

$$F(z)=2\pi zN^2(z)\vec{U}\nabla H/(H\omega_{M2}), \tag{2}$$

where $\vec{U}$ is the barotropic tidal current, H is the water depth, and ω_{M2} is the semidiurnal frequency [*Pichon et al*., 2013]. The vertically integrated forcing term from surface to bottom, $\int_0^H F(z)dz$, provides evidence of a preferential site for the internal tide generation along the shelf break between isobaths 200 and 1000 m (Figure 1). The mooring is located slightly shoreward of the generation region. Therefore, shoreward-propagating internal tides are expected to be observed at the mooring site.

2.2.2. Two-Layer Nonhydrostatic Model

Since ISWs are not generated in the hydrostatic HYCOM model, a two-layer nonhydrostatic model consisting of generalized Boussinesq equations derived by *Gerkema* [1996] is used to investigate generation and propagation of ISWs. The governing equations of two-dimension (y, z) in the two-layer model are

$$\begin{aligned}
&\frac{\partial u}{\partial t}+V\frac{\partial u}{\partial y}+u\frac{\partial U}{\partial y}+\frac{h_1-h_2}{H}v\frac{\partial u}{\partial y}-fv=0\\
&\frac{\partial v}{\partial t}+V\frac{\partial v}{\partial y}+v\frac{\partial V}{\partial y}+\frac{h_1-h_2}{H}v\frac{\partial v}{\partial y}+fu=-g'\frac{\partial \eta}{\partial y},\\
&\frac{\partial \eta}{\partial t}+V\frac{\partial \eta}{\partial y}+\frac{h_1-h_2}{H}\frac{\partial(v\eta)}{\partial y}+\frac{h_1h_2}{H}\frac{\partial v}{\partial y}+\frac{h_1^2v}{H^2}\frac{\partial h}{\partial y}-\frac{h_1h_2}{3}\frac{\partial^2}{\partial y^2}\left(\frac{\partial \eta}{\partial t}+V\frac{\partial \eta}{\partial y}\right)=W\Big|_{z=\eta},
\end{aligned} \tag{3}$$

where u (along-shore) and v (cross-shore) are the horizontal velocity difference between the upper and lower layers; η represents the vertical excursion of the interface; $H(y)$ is the water depth, h_1 is the reference thickness of the upper layer, and $h_2(y)=H(y)-h_1$; f is the Coriolis parameter; and g' is the reduced gravity. In addition, U (along-shore), V (cross-shore), and W (vertical) are the barotropic velocity components

$$U=-\frac{f}{\omega}\frac{Q\cos(\omega_{M2}t)}{H(y)}$$
$$V=\frac{Q\sin(\omega_{M2}t)}{H(y)}, \quad (4)$$
$$W=(z-h_1)\frac{Q\sin(\omega_{M2}t)}{H^2(y)}\frac{\partial H}{\partial y},$$

where Q is the barotropic tidal flux. Equation (3) is solved by a third order Adams Bashforth scheme and spatial first derivatives are computed using a fourth-order scheme [*Durran*, 1999]. To dampen artificial oscillations at the grid scale, a fourth-order spatial filter is added to the momentum equations.

If we do not consider nonlinear and nonhydrostatic effects and assume $\partial(U,V)/\partial y=0$, the horizontal propagation speed C_s of waves relative to the seabed is

$$C_s=C_w+V,$$
$$C_w\approx\sqrt{g'(h_1h_2/H)/(1-f^2/\omega^2)}, \quad (5)$$

where C_w is the wave phase speed and V represents the advection [*Pichon and Mazé*, 1990].

3. Character of Internal Tides

In this section, velocity and temperature data for the entire observation period are used to investigate the characters of the barotropic and internal tides. Results are compared to the HYCOM model. The horizontal velocity is decomposed into along-shore (u) and cross-shore (v) components, with the cross-shore direction defined toward 63° (see Figure 1).

3.1. Time Series

The current meter time series at three different depths clearly show a similar magnitude and phase with a dominant semidiurnal oscillation (Figures 3a–3c). This indicates that the velocity field is dominated by (semidiurnal) barotropic tides. Barotropic tidal currents are primarily directed cross-shore (Figure 3d), as shown by the barotropic M_2 tidal ellipse in Figure 1. Since the (semidiurnal) barotropic tide is the main component of the velocity field, we define the depth-averaged current given by the three current meters as the barotropic current. This observed barotropic current is in close agreement with that computed from the full depth profile in HYCOM (Figure 3d). The baroclinic current is computed as the total current minus the depth-averaged value. At 115 m depth, the semidiurnal baroclinic (internal tidal) current is visible at spring tide but shows a nonlinear character (Figure 3e). The model reproduces the variation of the internal tidal current observed at spring tide (before 6 September) well. At neap tide, the cross-shore barotropic tidal currents are largely weakened in the model and observations (Figure 3d). However, the cross-shore baroclinic current shows a much stronger decrease in the model than in the observations. This is due to the enhanced inertial (f) currents (period of ~16 h) at neap tide.

The internal tidal signals are best identified on time-depth maps of the observed temperature (Figures 4a and 4b). High-frequency nonlinear waves are also clearly visible on the map. The largest internal tide amplitude (vertical displacement) at spring tide exceeds 60 m. In this paper, amplitude of internal wave is defined by the largest vertical displace of isotherms in the thermocline (from the crest to trough). The internal tides are evidently nonlinear at spring tide. They have an asymmetric waveform relative to the symmetric sine-shape barotropic forcing, with deeply penetrating troughs and more rounded crests, as previously reported near the shelf break in Bay of Biscay [*Pingree and Mardell*, 1985]. On 1–4 September, the internal tides also show another asymmetry, with gentle drops and steep raises. At neap tide, internal tide displacements are obviously weakened, but high-frequency waves are still clearly visible although their amplitude is small (Figures 4c and 4d). Detailed observations and discussions for high-frequency nonlinear waves will be given in section 5.

To suppress the high-frequency nonlinear waves and better visualize the dominant features of internal tides at spring tide, a low-pass Butterworth filter with a cutoff frequency of 10 cpd is applied to velocity and temperature signals. A trough and two crests in each M_2-period can be clearly identified on the time-depth map of the filtered temperature signals (Figure 5a). Because of their semidiurnal periodicity, the trough and

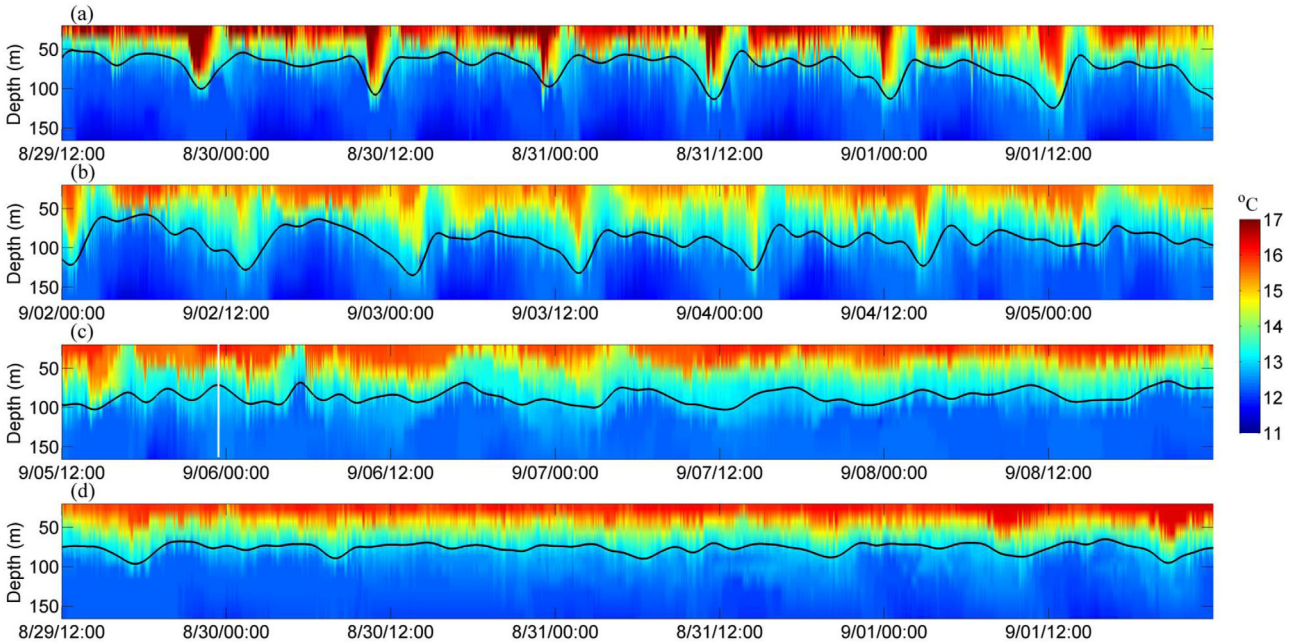

Figure 4. Time-depth maps of measured temperature data from 29 August to 12 September. Each plot is 3.5 day long. The low-pass filtered isotherm of 13°C (black line) is superimposed on depth-time maps. In Figure 4c, the vertical line indicates the boundary between spring and neap tides.

two crests are hereafter referred to as *T* (marked by black rectangles), C1 (marked by magenta vertical lines), and C2 (marked by green vertical lines). The HYCOM model reproduces *T*, C1, and C2 well. Their arrival times in model and observation data are nearly identical (Figure 5b). In the upper layer (20 m; Figure 5c), *T*(C1) generates a strong shoreward (seaward) current while an opposite current is observed in the lower layer (velocity averaged over the depths of 115 and 164 m; Figure 5d), which is consistent with vertical mode 1 waves. Indeed, the maximum displacement and zero velocity for mode 1 are at 54 m, implying that mode 1 velocities observed at 20 m and the depth below 100 m have a phase difference of 180° (see Figure 2c). For a vertical mode 1 depression (elevation), the velocity in the upper layer is the same as (opposite to) the direction of propagation. Therefore, one can deduce that *T* and C1 propagate onshore. Conversely, when the crests C2 arrive at the mooring site, baroclinic velocities in the upper layer are shoreward, while opposite velocity variation can be found in the lower layer (except for one event in the first tidal period on 29 August) suggesting that C2 may propagate offshore. Note that the advection by the barotropic tidal flow can change the propagation speed (C_s) of internal waves (equation (5)). Here shoreward or seaward (offshore) propagation refers to C_w. The above velocity field observations are mostly reproduced in the numerical model (Figures 5c and 5d).

3.2. Frequency Spectra

Spectra computed from observed temperature fluctuations and baroclinic velocities show the significant peaks at semidiurnal frequency (M_2) and higher tidal harmonics (e.g., M_4, M_6, M_8, M_{10}). The model reproduces these tidal harmonic peaks well (Figure 6a), although the semidiurnal peak of temperature spectra in the model is slightly higher than that in the observations (Figure 6b). In addition, a significant near-inertial peak is also observed in velocity spectra inferred from the observations but not in the model which is only forced with the barotropic tide.

4. Generation and Propagation of Internal Tides

In section 3, it was shown that both seaward and shoreward-propagating internal tides appeared at the mooring site. The HYCOM model reproduced observed internal tides with opposite propagating directions, although internal tides in the model are definitely generated offshore of the mooring site. One may thus ask why the seaward propagating internal tides appear onshore of their generation location. To answer this question and investigate the generation and propagation of internal tides on the shelf edge, the HYCOM

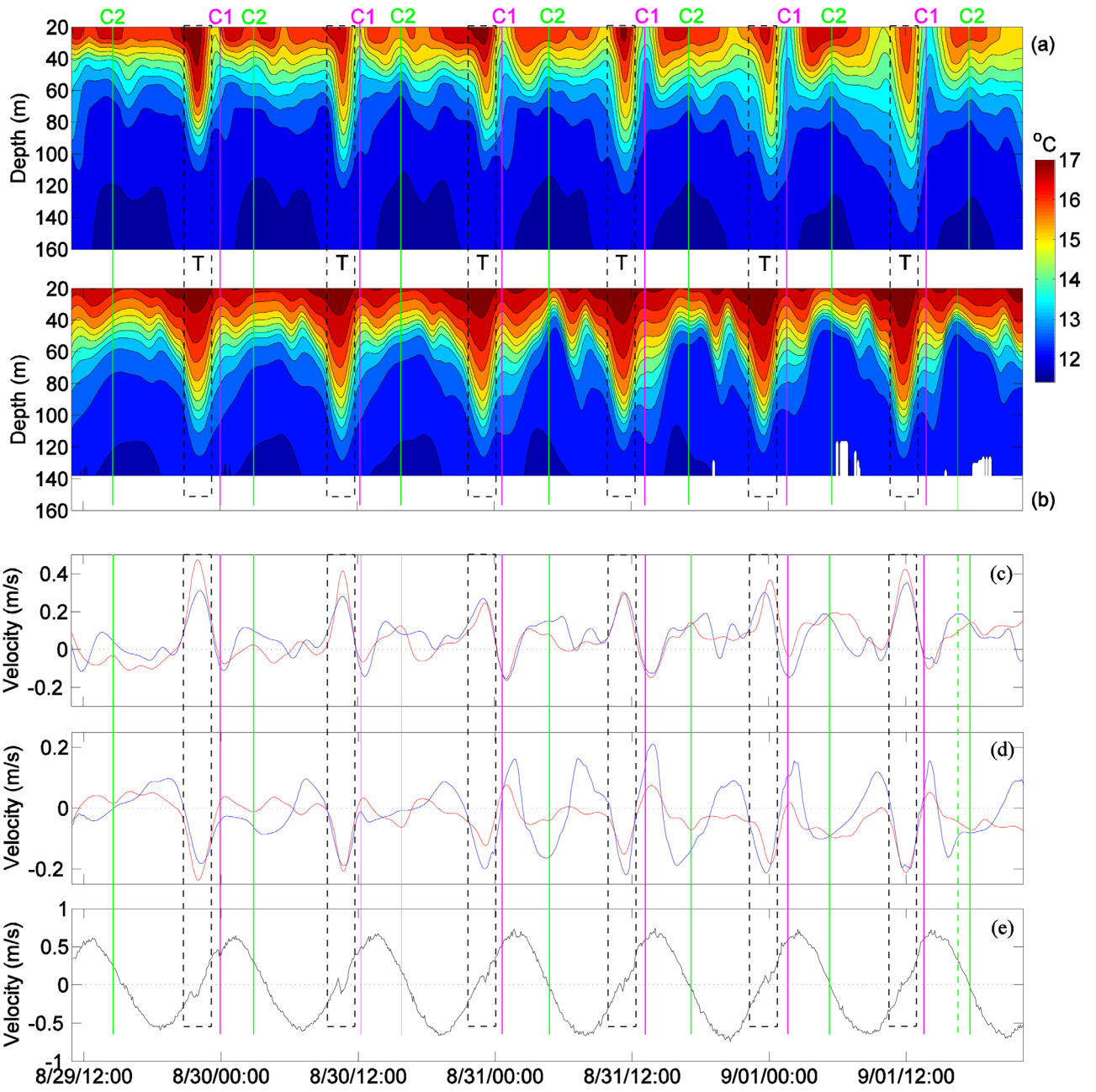

Figure 5. Time-depth maps of temperature at the mooring site between 29 August and 1 September obtained from (a) observation and (b) model. Cross-shore baroclinic velocity at depths of (c) 20 and (d) 164 m computed from observation (red) and model (blue). (e) Cross-shore barotropic velocity. Data from observation are low-pass filtered with cutoff frequency of 10 cpd. The rectangles indicate *T*. The vertical solid lines indicate the locations of two elevations C1 (magenta) and C2 (green). Note the difference in the occurrence time of C2 in the observations and in the simulations during the last semidiurnal period. From Figures 5c–5e, this occurrence time is displayed with solid (observation) and dashed (model) lines of the same color.

model results are further presented in this section. Here we mainly focus on the space-time evolution of the depth of the pycnocline. Figures 7a and 7b show its distribution along a cross-shore line passing through the mooring site in a full M_2-period at neap and spring tides, respectively.

4.1. Generation of Internal Tides

The simulations show the splitting of the generated internal tide into an onshore and an offshore component, as described in *Baines* [1982]. The internal tide at both spring and neap tides is generated at the shelf break between the mooring site and 7 kilometers (km) offshore of it (Figures 7a and 7b). At the generation

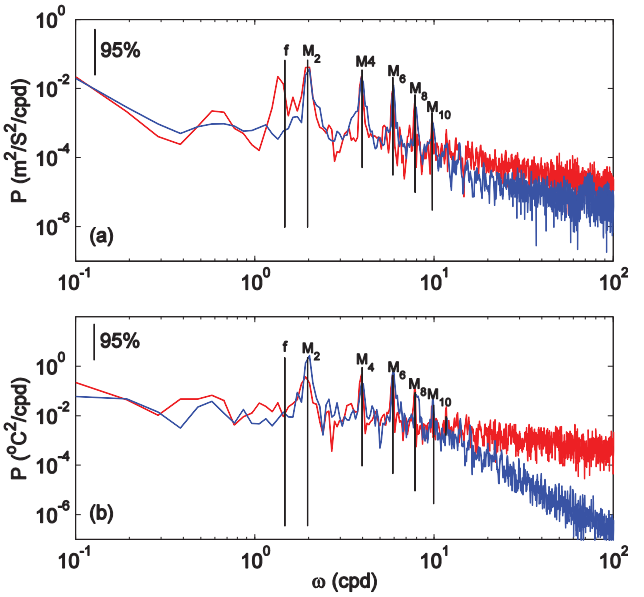

Figure 6. Depth-average power spectrums of (a) baroclinic velocities at depths of 20, 115, and 164 m and (b) temperature fluctuations at depths of 27, 42, and 57 m. Blue and red curves are the results of the model and observation, respectively. The solid thin vertical lines mark various harmonics (*f*, M_2, etc.). The 95% statistical significance level is indicated by the vertical bar near the top-left corner.

location, a pair of (onshore and offshore propagating) crests is separated from an elevation between $t = 2M_2/12$ and $t = 3M_2/12$, while a pair of (onshore and offshore propagating) troughs is separated from a depression after approximately half-M_2 period (between $t = 8M_2/12$ and $t = 9M_2/12$). Note that the time is referred to the same barotropic tidal phase at neap tides and spring tides (Figures 7c and 7d). The separation (generation) points of both crests and troughs at neap tide are ~7 km offshore of the mooring site (marked by the vertical dashed line; Figure 7a). The situation differs at spring tide, where the splitting of crests occurs nearly at the mooring site, while the separation point of troughs is still the same as that at neap tide. At spring tide, the passage past the mooring site of the onshore traveling crest between $t = 2M_2/12$ and $t = 3M_2/12$ and of the offshore traveling crest between $t = 5M_2/12$ and $t = 6M_2/12$ is consistent with the C1 and C2 signatures in Figure 5 (see the barotropic tidal phase in Figures 5e and 7d), respectively. Around $t = M_2/12$, a large depression crosses the mooring position (Figure 7b), corresponding to *T* signatures in Figure 5.

To illustrate the internal tidal splitting process with depth, the spatial distribution of the upper 12 isopycnals (covering the entire depth in the shelf) at spring tide are given in Figure 8. The elevation between $y = -5$ km and $y = 0$ separates into C1 and C2 during the period between $t = 2M_2/12$ and $t = 3M_2/12$ (Figures 8b and 8c). The depression left by the separation of C1 and C2 is very close to the mooring site and is clearly seen over the entire depth at $t = 3M_2/12$. The isopycnal displacement associated with the crest C2 increases with depth, suggesting that the offshore traveling internal tide is composed of multiple modes. As a result, the velocity shear associated with C2 is enhanced (Appendix A). Based on equation (5) and the horizontal wavenumber $K_h = \omega/C_w$, wavelength of the semidiurnal (M_2) interface tide near the mooring site is approximately equal to 30 km. This can be determined by the distance between two adjacent troughs in the pycnocline onshore of the mooring site (see Figure 7b). However, both C1 and C2 show a relatively small-scale feature. At $t = 3M_2/12$, the distance between C1 and the trough *T* onshore of it is about 8 km, which is much shorter than half M_2 wavelength. The distance (≈14 km) between *T* and the crest on its right side is approximately equal to half M_2 wavelength. Offshore of the mooring site, C2 and a small-scale crest at $y \approx -9$ km are only approximately 7 km apart. These relatively small-scale crests may be associated with higher tidal harmonics, since higher harmonics of M_2 imply a decrease in C_w (equation (5)) and an increase in K_h.

The trough separation position at spring tide differs from the crest one, and it occurs at $y \approx -7$ km, generating an elevation at the splitting position (marked by the vertical dashed line; Figures 7b and 8h–8l). Adjustment of the splitting position of crests may be associated with the large barotropic advection at spring tide. During the splitting of crests, the separation point may be onshore shifted by the strong onshore tidal current. As a result, the front face of the onshore traveling crest (C1) and the rear face of the offshore traveling crest (C2) steepen (see Figure 8c), leading to the generation of higher tidal harmonics. This also explains why the observed internal tide at the mooring site was asymmetric, with gentle drops and steep lifts (see Figure 4). For internal tides, such steepening is theoretically caused by the quasi-nonlinearity, namely the advection of the baroclinic tide by the barotropic tide [*Pichon and Mazé*, 1990].

4.2. Propagation of Internal Tides

At spring tide, the splitting position of internal tides is not fixed but evolves with the phase of the barotropic tide. This suggests important influence of the barotropic advection on the internal tidal generation,

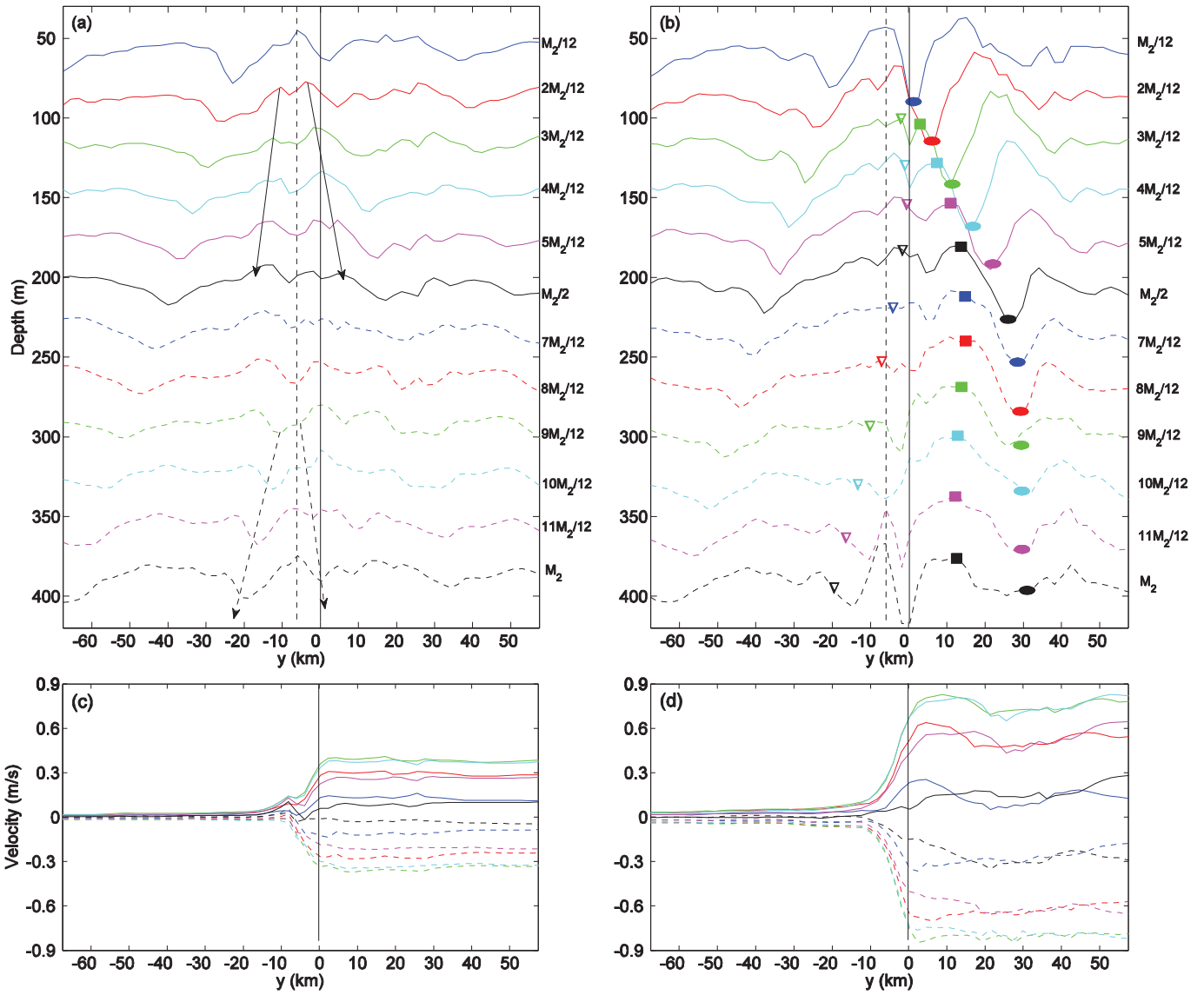

Figure 7. (a and b) Spatial distribution of the pycnocline depth and (c and d) the cross-shore barotropic velocity along *y* direction shown in Figure 1 for a complete M_2-cycle at (a and c) neap and (b and d) spring tides in HYCOM model. Time interval between two adjacent curves is ~1 h. The same M_2/12 period is indicated by the same color. The last half M_2-cycle is discriminated by the dashed curve. The vertical solid line marks the location of the mooring site ($y = 0$ km), while the vertical dotted line indicates the splitting (generation) location of crests and troughs. In Figures 7a and 7b, the vertical offset for displacement is 30 m. In Figure 7a, the propagation routes of two crests and two troughs are marked by the solid and dashed arrows, respectively. In Figure 7b, ellipses, squares, and triangles indicate the locations of *T*, C1, and C2 computed by equations (5) and (6), respectively.

especially the generation of nonlinear internal tides consisting of the fundamental M_2 and higher tidal harmonics. Also, the strong barotropic advection modifies internal tidal propagation significantly. The onshore propagation of C1 and *T* is stopped by the offshore barotropic current during the second half of the M_2-period. The seaward traveling crest (C2) is even advected shoreward in the first half M_2-cycle corresponding to the onshore tidal velocity (Figure 7b). Based on equation (5), the progression of traveling internal tides in a two-layer system can be estimated as

$$y(t) = y_0 + \int_0^t C_s(y)dt'. \tag{6}$$

The linear model (equations (5) and (6)) with $\omega = M_2$ can estimate well the propagation of *T* in the full M_2-period (Figure 7b), but it fails to reproduce propagation of C1 and C2 (not shown). Instead, the linear model

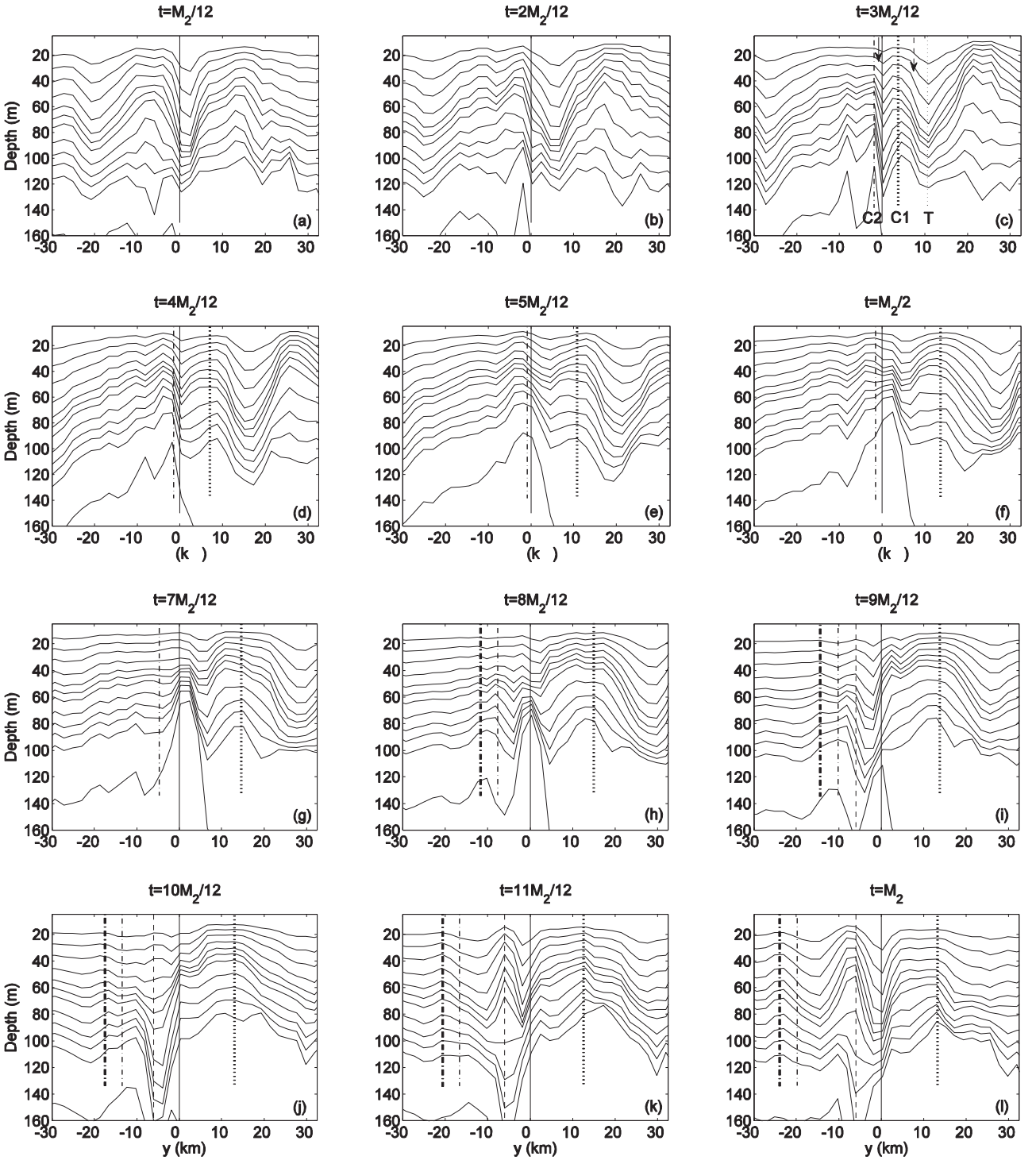

Figure 8. Spatial distribution of the upper 12 isopycnals layers at spring tide for the M_2-cycle shown in Figure 7b. The vertical solid lines indicate the location of the mooring site. In Figures 8c–8l, the heavy dotted line and light dash-dotted line indicate the locations of C1 and C2 computed by equations (5) and (6), respectively. Dashed and solid arrows indicate the front face of C1 and the rear face of C2, respectively. In Figures 8h–8l, the heavy dash-dotted line marks the actual position of C2. In Figures 8i–8l, the vertical dashed line indicates the trough splitting location.

with $\omega >= M_4$ not only models well the propagation of C1 in the full M_2-period, but reproduces the onshore advective propagation of C2 in the first half M_2-cycle (Figure 7b). This may be explained by the fact that C1 and C2 are mainly represented by higher harmonics of the tides that were evidenced by the spectrum of Figure 6 and their spatial scales shown in Figure 8. Note that f/ω is close to zero in equation (5) when

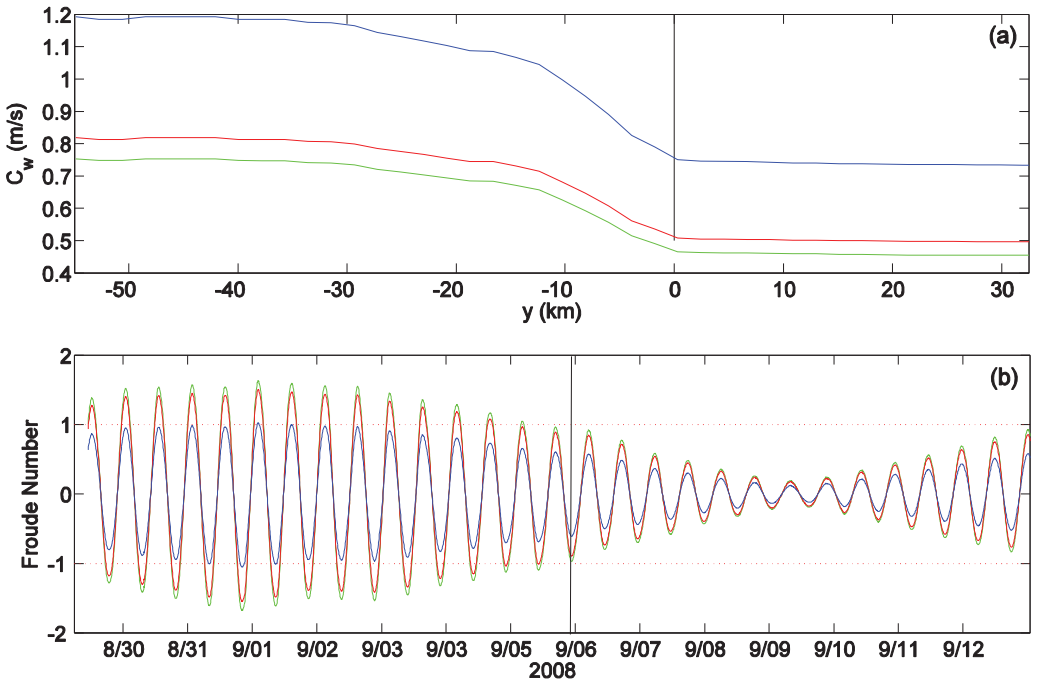

Figure 9. (a) Phase speeds (C_w) of M_2 (blue) and M_4 (red) waves computing from equation (5) along y direction in shown Figure 1. The green curve is the result of equation (5) with $f/\omega = 0$. The verical line indicates the mooring site. (b) Time series of Fr based on C_w of M_2 (blue) and M_4 (red) waves. The green curve is the result in the case of $f/\omega = 0$. The vertical line indicates the boundary between spring and neap tides. Two horizontal lines indicate the critical values.

$\omega >= M_4$. The propagation speed of higher tidal harmonics (M_4 and higher) is thus approximately equal to the speed in the case of $f/\omega = 0$ (Figure 9a). Although the large trough T is clearly nonlinear, it is phase locked with the fundamental M_2 harmonic. Note that the distance of two adjacent troughs in the shelf is a M_2 wavelength (see Figure 7b). Therefore, its propagation can be modeled by equations (5) and (6) with $\omega = M_2$. After the generation at $t = 3M_2/12$, C1 is gradually widened when they propagate onshore (Figures 7b and 8c–8l). This can be attributed to the separation of M_2 and higher harmonics because of their different propagation speeds (Figure 9a).

The onshore advective propagation of the crest C2 between $t = 3M_2/12$ and $t = M_2/2$ is better evidenced here with the complete depth profile (Figures 8c–8f). The off-shore traveling internal tide has a complex vertical structure near the generation point revealing the presence of several vertical modes with different phase speed. Once C2 propagates away from the generation position (Figures 8g–8l), modes separates because of different propagation speeds. This is not taken into account by equations (5) and (6) and a small shift (∼5 km) between the predicted position and the actual C2 position (determined by eye) emerges in the pycnocline (40–60 m) after $t = 7M_2/12$ (Figures 8h–8l). The mode 1 propagates faster than higher modes and C2 takes the form of single vertical mode 1. The predicted phase speed in equations (5) and (6) is then correct since the shift between actual and predicted position does not evolve between $t = 8M_2/12$ and $t = M_2$.

To confirm whether propagation of C2 is reversed by the barotropic tidal current in the entire observation period, we compute an internal Froude number near the generation site of C2, $Fr = V/C_w$ [*Hibiya*, 2004]. Based on equation (5), $Fr > 1$ (< -1) means the offshore (onshore) propagating wave may be swept onshore (offshore) to the shelf (sea). Since the crest split occurs near the mooring site, time series of the barotropic tidal velocity in HYCOM model at the mooring site is used when calculating Fr. The results show that Fr is between -1 and 1 in the entire observation period for the M_2 harmonic, suggesting that the offshore traveling M_2 internal tide cannot be advected onshore. However, $Fr > 1$ occurs in most tidal cycles at spring tide for higher tidal harmonics and all waves in the case of $f = 0$ (Figure 9b). At neap tide, Fr for all waves is smaller than one, indicating that C2 is advected onshore only at spring tide.

5. High-Frequency Nonlinear Internal Waves

In this section, we describe in detail the features of the high-frequency nonlinear internal waves observed in the field data, and discuss their generation mechanism in light of the two-layer nonhydrostatic model and HYCOM model results.

5.1. Wave Properties

A time-depth map of 24 h temperature data (two M_2-cycles) during spring tide clearly shows mode 1 high-frequency nonlinear waves. These waves have different amplitudes. To distinguish them, waves with $|\eta| > 20$ m and $|\eta| < 20$ m are hereafter referred to large and small amplitude high-frequency nonlinear waves, respectively. We mainly focus on these large nonlinear waves which are referred to as ISWs in the following. In each tidal period at spring tide, all observed ISWs appear in the trough *T* and the rear faces (marked by horizontal arrows) of C1 and C2, respectively (Figure 10a). Therefore, ISWs are classified into three types of wave packets depending on where they appear. Next, we describe the character of these packets in detail.

In the trough *T*, two ISWs generate an onshore current in the upper layer (Figures 10a and 10b; also see Figures 10f and 10i). Since the ISWs are mode 1, an opposite velocity direction is observed near the bottom (164 m). The velocity anomalies caused by the ISWs and *T* have the same sign, suggesting the same propagation direction. Moreover, the along-shore current associated with ISWs and *T* is significantly weaker than the cross-shore velocity, implying that both of them propagate onshore onto the shelf. Hereafter, the ISW packet which is located in the troughs *T* is referred to as S_T. During the entire observation period, we identify five S_T occurrences.

After *T* (S_T), several large nonlinear waves (ISWs) and a number of small amplitude waves are observed between C1 and C2 (Figures 10a and 10d). These ISWs appear in the rear face of C1, inducing a shoreward velocity anomaly in the upper layer (Figures 10b and 10g). Since these waves have a very short period, they are not resolved by the velocity record of the lower layer due to a lower time resolution (5 min). This packet of ISWs appearing in the rear face of C1 is hereafter referred to as S1. In the entire observation period, eight S1 are observed during eight tidal periods at spring tide. Based on the high-frequency velocity record at a depth of 20 m and the current velocity shear obtained from HYCOM, the propagation direction θ of ISWs in S1 is estimated (Appendix A). The results show that S1 propagate northeastward (Figure 11); that is, they travel shoreward across the shelf, in a similar way as C1.

Between C2 and S_T, one or multiple ISWs followed by a number of small amplitude high-frequency waves can be seen (Figures 10a and 10e). Note that only one large nonlinear wave is seen in the rear face of C2 within two tidal cycles as shown in Figure 10, but more than one ISW is observed in some other tidal cycles at spring tide. These large ISWs generate an offshore velocity anomaly in the upper layer, with an opposite velocity anomaly in the lower layer (Figures 10b and 10h). The packet consisting of ISWs observed in the rear face of C2 almost appears at every M_2-cycle at spring tide. Hereafter, these packets are referred to as S2. A total of 13 S2 are observed at spring tide. These packets propagate offshore, which is the same as C2 (Figure 11). The θ estimation for S2 shows that the propagation direction of S2 is nearly opposite to that of S1.

The amplitude of the largest ISW in both S1 and S2 exceeds 40 m. The first ISW in most of all observed ISW packets has the largest amplitude, as shown in Figure 10. In addition, the current fluctuations observed during ISWs in S2 suggest an evident along-shore current whose amplitude is comparable to the cross-shore component (see Figure 10c), although the barotropic tides propagate cross-shore. This along-shore direction of the current anomalies may not represent the intrinsic ISW direction but may be caused by the superposition of the vertical advection of the background shear current and the intrinsic signature of the ISWs (see Appendix A).

At neap tide, large amplitude solitary waves are no longer observed. Instead, the entire tidal period is filled with a number of small amplitude nonlinear internal waves and the classification into the three wave packets S1, S2, and S_T no longer holds (not shown).

5.2. Generation Mechanism

In section 5.1, three types of ISW packets at spring tide were identified. Like internal tides, these packets show bidirectional (shoreward and seaward) propagation in a tidal period. Especially, all large amplitude

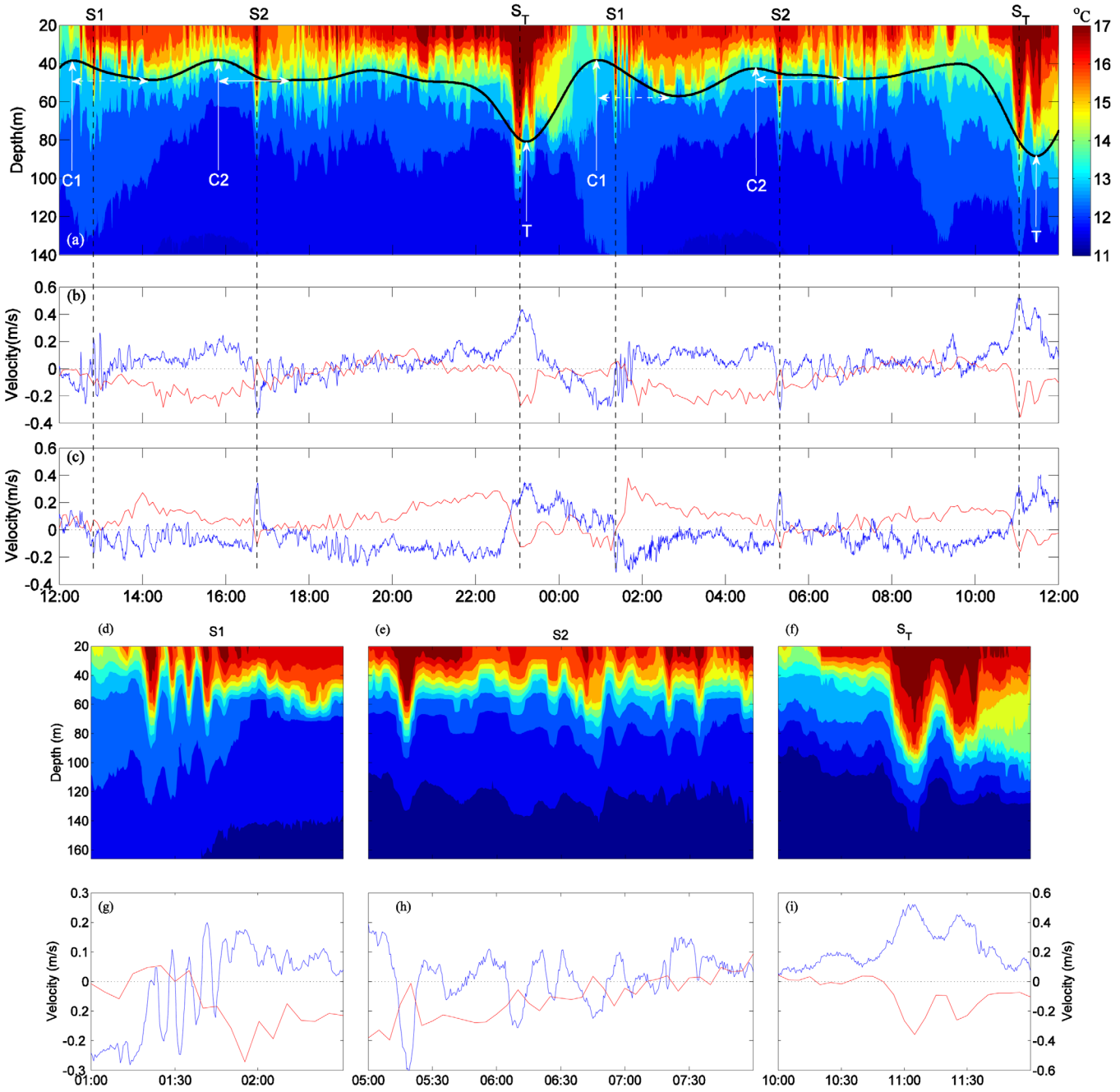

Figure 10. (a) Time-depth map of temperature, and (b) cross-shore and (c) along-shore baroclinic velocities from 12:00/30/8 to 12:00/31/8. Figures 10d–10f and 10g–10i are details of Figures 10a and 10b (S1, S2, and S_T) in the second semidiurnal cycle, respectively. Vertical dashed lines in Figures 10a–10c indicate ISW packets. A low-passed interface depth (black curve) is superimposed on Figure 10a, where the white vertical arrows indicate locations of C1, C2, and *T*. The horizontal dashed and solid arrows indicate the rear faces of C1 and C2, respectively. In Figures 10b and 10c, the blue and red lines are results of the upper (20 m) and low (164 m) layers, respectively.

high-frequency nonlinear internal waves appear in the internal tidal troughs (*T*) or near the rear face of internal tidal crests C1 and C2, and show a propagation direction that is the same as either *T*, C1, or C2. This suggests a generation mechanism of ISWs through a nonlinear steepening of internal tides. In order to get insights on this mechanism, we performed simulations with the nonhydrostatic two-layer model. As well, we expect to understand why ISWs do not all propagate in the same direction.

The domain of the two-layer model is set to be from −400 to 400 km with a resolution of 50 m (Figure 12). The shelf edge (the mooring site) is located at $y = 0$ km. An ideal two-dimension topography fitted to the

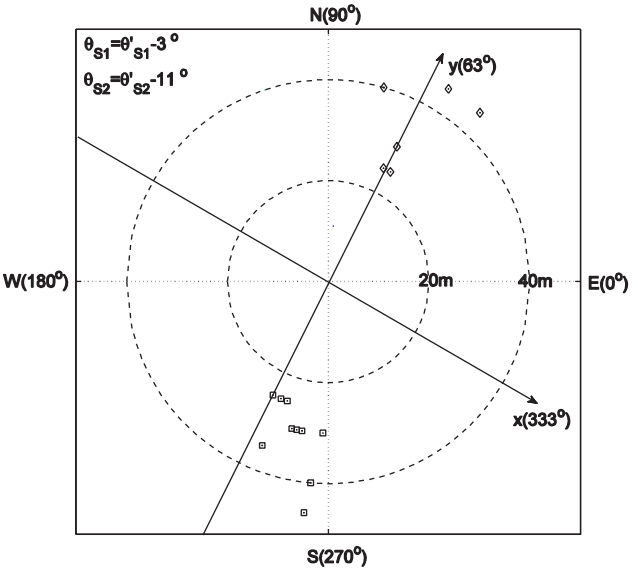

Figure 11. The propagating direction θ of six S1 (diamonds) and 10 S2 (squares) based on equation (A1) with the background velocity shear. Distance from diamonds/squares to center represents amplitude of the largest ISW in each S1/S2 packet. Two circles indicate amplitudes of 20 and 40 m. The error is shown in the top-left corner.

Bay of Biscay is exploited: $h(y) = 170$ m on the shelf and $h(y) = 4000$ m in the deep ocean. On the slope, $h(y)$ varies within a length of 50 km. Its variation is obtained using a cubic interpolation based on three given depths: $h(-50$ km$) = 4000$ m, $h(-12$ km$) = 1200$ m, and $h(0) = 170$ m. The above configuration is similar to that of *Gerkema* [1996]. Before running the model, we extract two parameters from the stratification obtained from the fixed site: $h_1 = 50$ m and $g' = 5.5 \times 10^{-3}$m s^{-1}. The barotropic flux Q of the model is the sum of M_2 (= 80 m^2/s) and S_2 (= 39 m^2/s) components. We checked that U at $y = 0$ km in the model is consistent with the barotropic current at the mooring site (Figure 13a). The model is initially at rest. The barotropic tidal forcing starts five M_2-periods before the initial observation time at the mooring site. Time series of interface displacement (η) and cross-shore velocity transition (v) at $y = 0$ km are shown in Figure 13. The interface displacement inferred from temperature data and velocity difference between depths of 20 and 115 m as the field observation are shown as well as for comparison.

Although the configuration of the two-layer system is much more ideal than the HYCOM model, it also reproduces the general variation of the observed η and the observed velocity difference between the upper and the lower layers at spring tide (Figures 13b and 13c). Large depressions are clearly identified at spring tide. Their amplitudes and arrival time, along with velocity variation they generate, are consistent with those of observed for T (Figures 13b and 13c). Due to the balance of nonlinear and nonhydrostatic effects, a group of ISWs emerges from troughs in the model (Figures 13b and 13e) [*Gerkema and Zimmerman*, 1995]. The observed S_T packets can be thus attributed to nonlinear steepening of T. In addition to T, the seaward propagating internal tidal crest C2 is also generated in the model, although their arrival time in the model and data have a slight shift in phase (Figure 14). In the rear face of C2, the first seaward traveling ISW begins to emerge and its appearance time is nearly consistent with the first ISW in the seaward propagating S2 packet (Figures 13e and 13f). On the other hand, the crest C1 following T is not well simulated in the model (Figure 14). As a result, the other observed onshore traveling ISW packet associated with C1, namely S1, is not excited in the model (Figure 13).

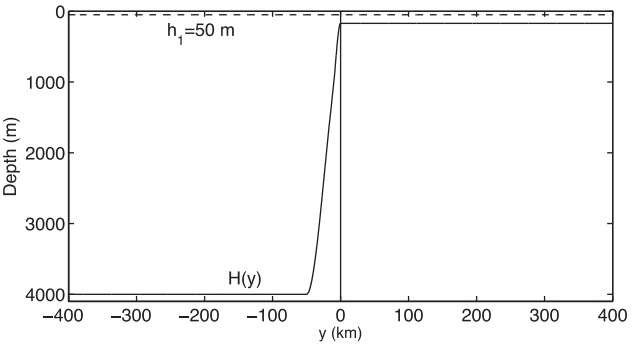

Figure 12. The topography (solid) and interface depth (dashed) used in the two-layer model. The vertical line indicates the shelf edge ($y = 0$) corresponding to the mooring site.

To further show generation and propagation of onshore and offshore propagating ISWs in the two-layer model, the spatial distribution of interface displacements is shown in Figure 15. The generation of internal tides in the two-layer model is similar to HYCOM results: two crests (C1 and C2) split between $t = 2M_2/12$ and $t = 3M_2/12$ near the mooring location (Figure 15a). The offshore traveling C2 is first swept onshore of the mooring site by the onshore barotropic current between $t = 3M_2/12$ and $t = M_2/2$ and then back offshore of the mooring

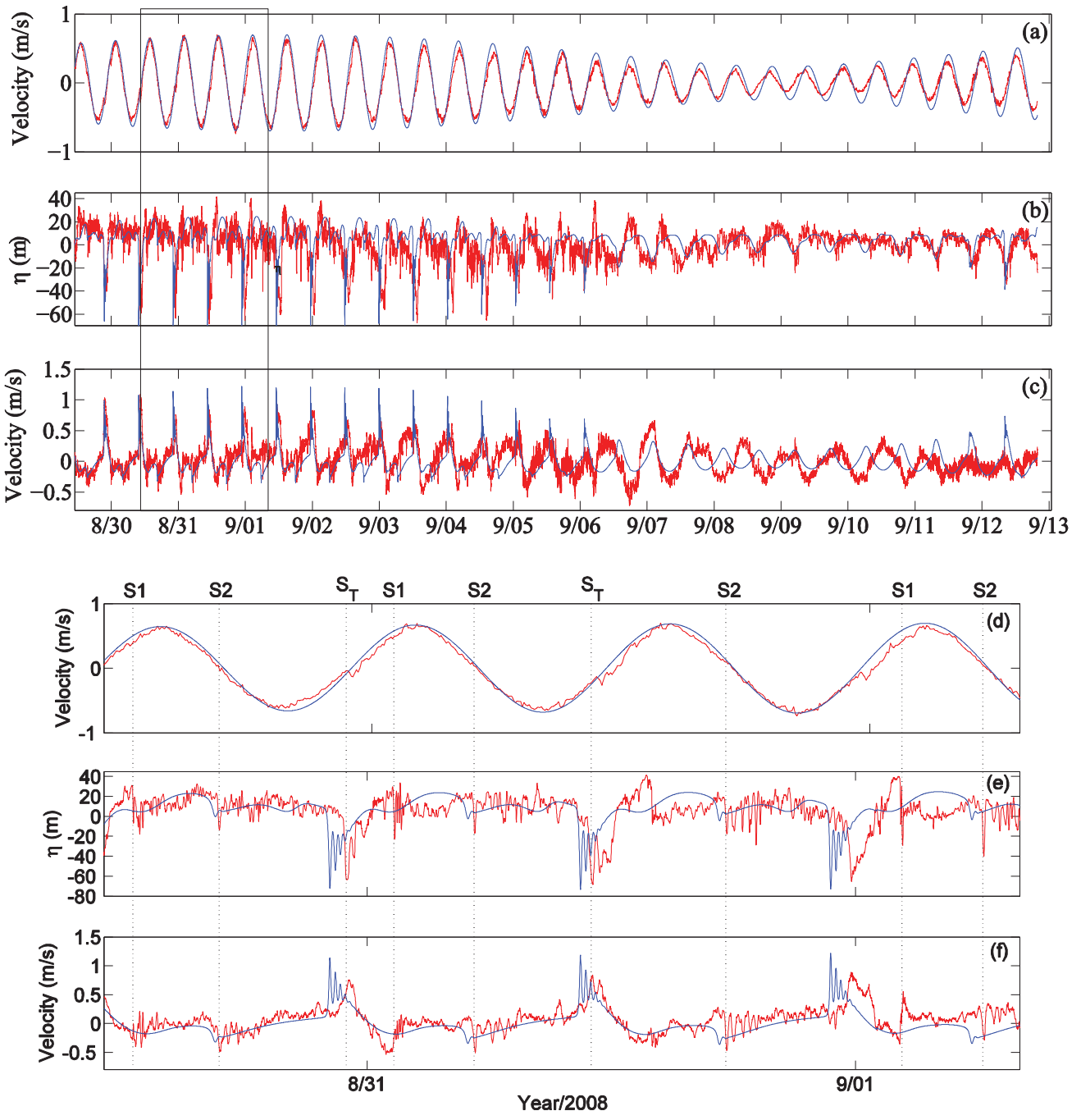

Figure 13. Time series of (cross-shore) (a) barotropic current, (b) interface displacement, and (c) (cross-shore) velocity difference between upper and low layers at $y = 0$ km in the two-layer model (blue). As a comparison, the observation result is plotted (red). (d–f) Zoom map of Figures 13a–13c, respectively. The rectangle indicates the period range in Figures 13d–13f, where the vertical dotted lines show arrival time of the first observed ISW in S1, S2, and S_T packets. The velocity difference of the mooring data is computed from velocity at depths of 20 and 115 m, similarly for Figure 14b.

site after $t = M_2/2$. It is during the latter process that the seaward traveling ISW packet, namely S2, emerged. This explains why S2 appears following C2 at the mooring site. Between $t = 10M_2/12$ and $t = 11M_2/12$, a depression, namely *T*, is generated offshore of the mooring site and propagates onshore (Figure 15a). During its shoreward propagation, the onshore going ISWs (S_T) are excited via nonlinear steepening of the trough *T*. The other group of onshore traveling ISWs, namely S1, is not reproduced in the model due to the limitation of the nonhydrostatic model that is only 2-D and two-layer. In addition, we note that internal tides can also be effectively generated at the southern continental slope, namely the Spanish slope (see

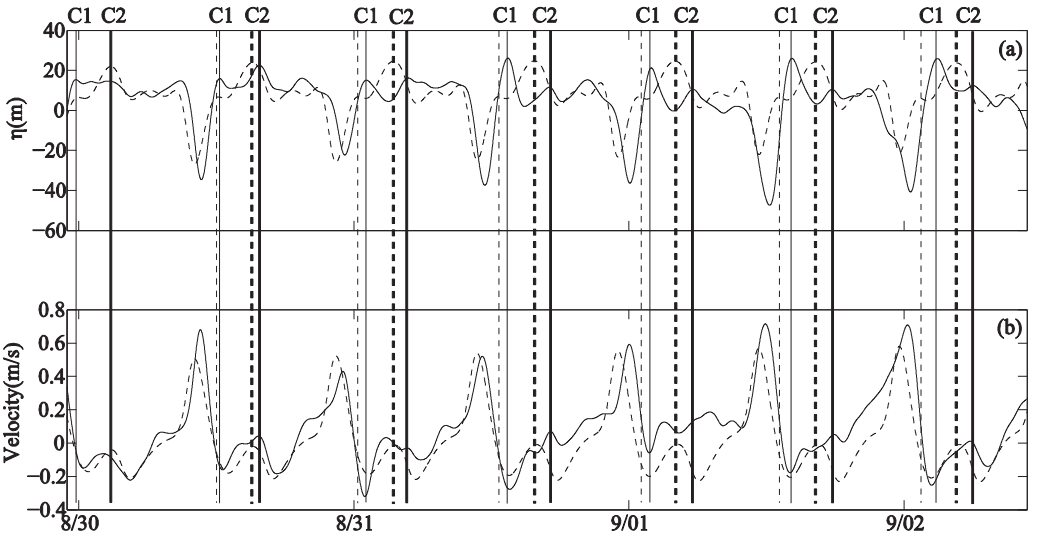

Figure 14. Time series of low-pass filtered (a) interface displacement and (b) velocity difference from 30 August to 2 September. The solid and dashed curves are the results of the two-layer model and observation, respectively. The vertical lines indicate locations of C1 (light) and C2 (heavy). If their locations for the same signature in the model and data have a slight shift, the dotted line is for the model while the solid line is for the observations.

Figure 1). This provides another source of internal tides which may propagate northward onto the northern shelf edge and evolve into ISWs trains there [*Nash et al*., 2012].

6. Summary and Discussion

Although internal tides in the Bay of Biscay have been extensively studied, we report the first high-frequency in situ observations over a full spring neap cycle which allow us to characterize ISWs generation near the shelf break. In addition to these observations, we used a hydrostatic HYCOM model and a two-layer nonhydrostatic model to investigate the generation and propagation of nonlinear internal tides and ISWs on the Armorican shelf edge in the Bay of Biscay. The approximately 14 day long temperature and current observations show internal tides with opposite propagation directions (seaward and shoreward) in an M_2-cycle during spring tide. Numerical results indicate that advection caused by the strong barotropic flow affects the internal tidal generation and propagation significantly and is essential for the seaward traveling internal tides to appear shoreward of their generation location.

The observations revealed a complicated pattern for high-frequency nonlinear internal waves of large amplitude (up to 40 m): several packets with ISWs are encountered over a tidal period. Furthermore, like internal tides, the seaward and shoreward traveling ISWs are also observed at the same location. Combining field data and nonhydrostatic numerical results, we show that the seaward and shoreward going ISWs are excited via nonlinear steeping of offshore and onshore propagating internal tides generated on the shelf break, respectively. Another possible explanation for the seaward propagating ISWs (S2) is that they may be generated on the northern shelf and propagate seaward to the mooring site. On the northwestern shelf of the mooring site, there are some small-scale hills where the largest forcing term is about 1/3 of that on the slope (see Figure 1). However, no large seaward propagating internal tides ($>$20 m) in HYCOM model are identified in these areas, while the largest amplitude of observed seaward traveling ISWs reaches 40 m. To test whether these large amplitude ISWs are generated near these small-scale topography, we recalculate the two-layer nonhydrostatic model with the largest forcing term which is 1/3 of that in the previous experiment in section 5.2. As expected, the internal tide generated is weak ($<$15 m) and there is no generation of ISWs in this numerical experiment (not shown). Therefore, this small-scale topographic feature on the shelf is unlikely to be the generation location of S2 waves. Furthermore, S2 propagates south-southwest. If they are generated on the self, their generation location is more likely in the north-northeast of the mooring site. But in these regions, no significant forcing term is seen.

In addition, there is a shoreward traveling solitary wave packet (S1) which is not reproduced in the nonhydrostatic model. This one may originate from internal tides generated on the Spanish slope or from 3-D and

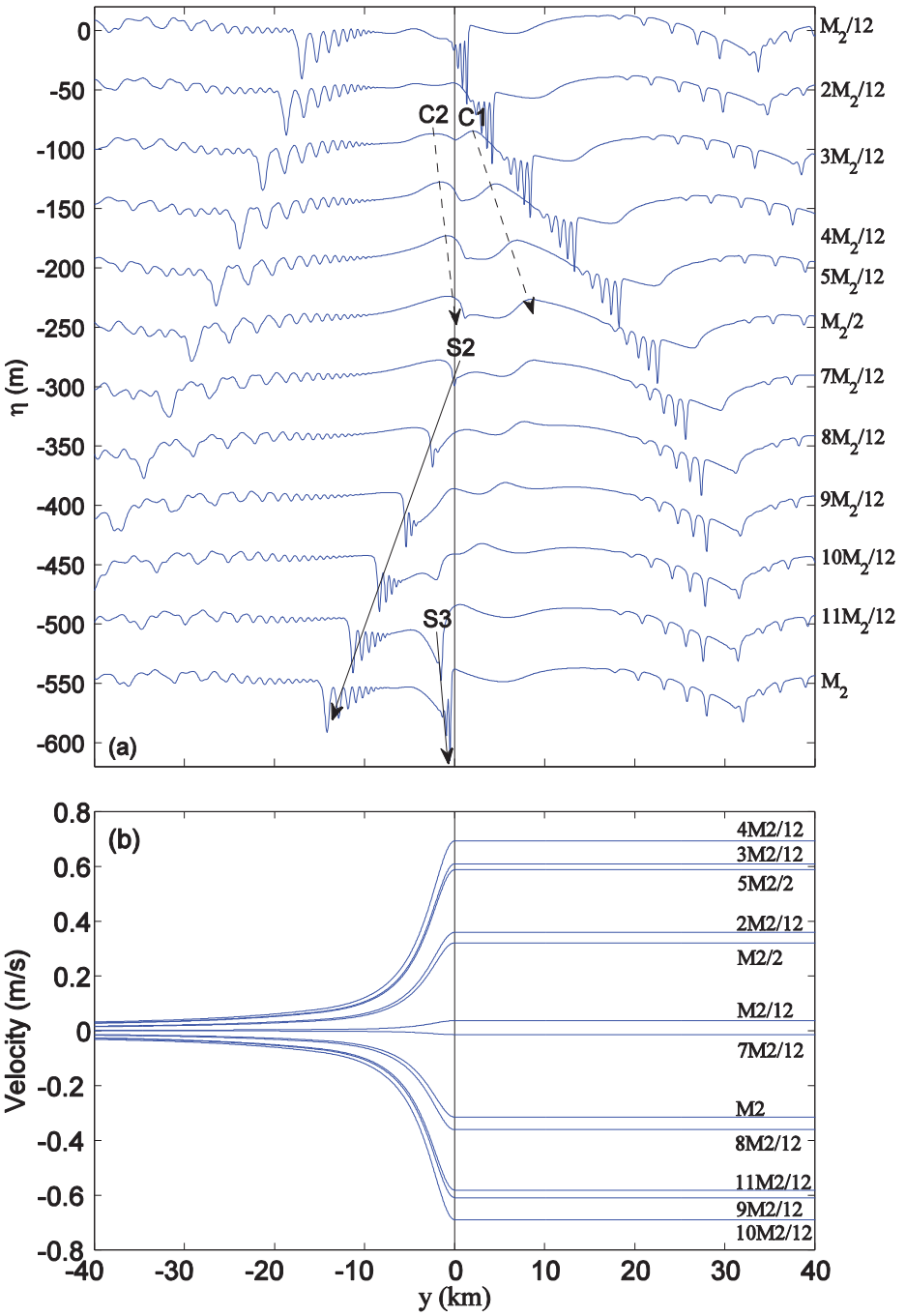

Figure 15. (a) Spatial distribution of interface displacement computed from the two-layer model for a complete M_2-cycle at spring tide. The dashed arrows indicate the propagation of C1 and C2. The solid arrows indicate the possible generation and propagation of S2 and S_T. (b) Similar to Figure 15a but for cross-shore barotropic velocity. The vertical line indicates the location of $y = 0$ km.

stratification effects not taken into account in the two-layer model. In the future, 3-D nonhydrostatic numerical simulations with real topography and stratification and additional moored data across the shelf are needed to provide further insights on the generation process of these ISWs.

Appendix A: Estimation of the Propagation Direction of Solitary Waves

The propagation direction θ of ISWs is estimated using the current meter record at depth of 20 m and the following method:

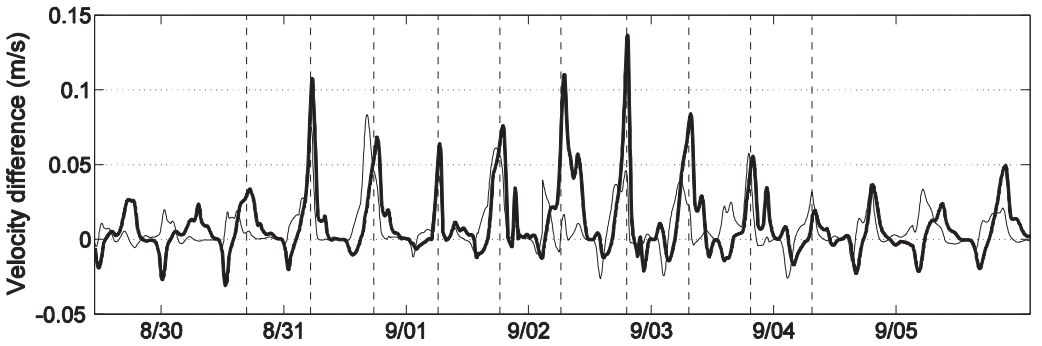

Figure A1. Time series of zonal (heavy) and meridional (light) velocity difference between depths of 10 and 20 m in the HYCOM model. Vertical lines indicate arrival time of the first observed ISW in S2.

$$\begin{aligned}\theta &= \arctan\left(v_0/u_0\right)\\ &\approx \arctan\left[(u_m - U_b)/(v_m - V_b)\right],\end{aligned} \tag{A1}$$

where u_0 and v_0 are the zonal and meridional velocity anomalies, (u_m, v_m) are the measured velocities when solitary waves cause the maximum displacement at the mooring site, and (U_b, V_b) are the corresponding background velocities. The background velocity is computed by

$$[U_b, V_b] = [(u_{m1} + u_{m2})/2, (v_{m1} + v_{m2})/2], \tag{A2}$$

where (u_{m1}, v_{m1}) and (u_{m2}, v_{m2}) are the velocities before and after ISWs, respectively and their time interval is an ISW period. The velocity anomaly (u_0, v_0) we define results from two contributions:

$$u_0 = u_s + [U_b(z - \eta) - U_b(z)]. \tag{A3}$$

The first contribution (u_s) is the velocity directly induced by the ISW and the other one is vertical advection of the background velocity by the ISW [*Chang et al.*, 2010]. The second contribution can be neglected providing that the background vertical shear is small. Since S_T emerge from the rough T generating a strong onshore current, the background current is difficult to be effectively extracted in (A2). (A1) cannot thus be used to estimate θ of ISWs in S_T, but their propagation direction can be well identified based on T. During S1 and S2, variation of these background currents in an ISW period (5–15 min) is small. (A2) can therefore extract the background currents effectively unless the background shear in (A3) is large. Here only θ of S1 and S2 packets is estimated.

The random noise of velocity measurement may affect the estimate of θ. To reduce this effect, (A1) is computed only for ISWs with

$$[(u_m - U_b)^2 + (v_m - V_b)^2]^{1/2} > 0.2 \text{ m/s}. \tag{A4}$$

Often there is more than one ISW in a packet that meets this criterion. To further reduce the instrument error, the propagation direction of the packet is defined as θ averaged over all available ISWs in a packet. There are six S1 and 10 S2 which satisfy (A4). All of these packets appear before 4 September, during which the background currents are dominated by the barotropic and baroclinic tidal currents. The strong baroclinic tides may generate strong vertical shear, the approximation in (A1) may then lead to significant errors in estimating θ of S1 and S2 [*Chang et al.*, 2010; *Mirshak and Kelley*, 2009]. Unfortunately, we cannot estimate the vertical shear from our sparse velocity measurement. In section 3.1, it is shown that the HYCOM model reproduces the observed baroclinic currents well before 4 September (see Figure 3e). Velocity shear in the model is instead used to estimate the term $U_b(z - \eta) - U_b(z)$.

The model data show that large shear currents associated with internal tides mainly appear during S2 (Figure A1). This is associated with the seaward traveling high-mode internal tides. So, θ estimation for S2 derived from (A1) without the velocity difference may have relatively large errors. The error for θ estimation of ISWs in S1 and S2 is computed by

$$Er = \theta - \theta', \tag{A5}$$

where θ and θ' are the estimated results derived from (A1) with and without the velocity shear, respectively. In addition, the HYCOM results also show that velocity difference in u direction during S2 is often large. For

a cross-offshore propagating ISW ($u_s < 0$, $v_s < 0$), if the velocity difference in u direction is large enough to change the direction of the velocity anomaly, namely $u_0 > 0$, the measured velocity may show a large along-shore current. This may explain why there is often a large along-shore velocity during S2 though the barotropic tides propagate cross-shore, as shown in Figure 10c.

Acknowledgments
Most of this work was performed at LOCEAN-UPMC. It was supported by the French National Research Agency "ANR" in the framework of the EPIGRAM project. The first author was also funded by the projects XDA11010202 and 41376022. We thank Theo Gerkema for providing the two-layer nonhydrostatic model and useful comments on the model configuration. The authors also acknowledge the assistance from the captain and the crew of the French research vessel "Pourquoi Pas" and Pascale Lelong for editing this paper. Data used for producing the results herein may be requested by contacting the first author (xhxie@scsio.ac.cn).

References

Baines, P. G. (1982), On internal tide generation models, *Deep Sea Res., Part A*, *29*, 307–338.
Bleck, R. (2002), An oceanic general circulation model framed in hybrid isopycnic-cartesian coordinates, *Ocean Modell.*, *4*, 55–88.
Chang, M. H., R. C. Lien, Y. J. Yang, and T. Y. Tang (2010), Nonlinear internal wave properties estimated with moored ADCP measurements, *J. Atmos. Oceanic Technol.*, *28*, 802–815.
Durran, D. R. (1999), *Numerical Methods for Wave Equations in Geophysical Fluid Dynamics*, Springer.
Gerkema, T. (1996), A unified model for the generation and fission of internal tides in a rotating ocean, *J. Mar. Res.*, *54*, 421–450.
Garrett, C., and E. Kunze (2007), Internal tide generation in the deep ocean, *Annu. Rev. Fluid Mech.*, *39*, 57–87.
Gerkema, T., and J. T. F. Zimmerman (1995), Generation of nonlinear internal tide and solitary waves, *J. Phys. Oceanogr.*, *25*, 1081–1094.
Gerkema, T., F. P. A. Lam, and L. R. M. Maas (2004), Internal tides in the Bay of Biscay: Conversion rates and seasonal effects, *Deep Sea Res., Part II*, *51*, 2995–3008.
Gill, A. E. (1982), *Atmosphere-Ocean Dynamics*, 662 pp., Academic Press, N. Y.
Hibiya, T. (2004), Internal wave generation by tidal flow over a continental shelf slope, *J. Oceanogr.*, *60*(3), 637–643.
Holloway, P. E., E. Pelinovsky, T. Talipova, and B. Barnes (1997), A nonlinear model of internal tide transformation on the Australian north west shelf, *J. Phys. Oceanogr.*, *27*, 871–891.
Lam, F. P. A., L. R. M. Maas, and T. Gerkema (2004), Spatial structure of tidal and residual currents as observed over the shelf break in the Bay of Biscay, *Deep Sea Res., Part I*, *51*, 1075–1096.
Leaman, K., and T. Sanford (1975), Vertical energy propagation of internal waves: A vector spectral analysis of velocity profiles, *J. Geophys. Res.*, *80*, 1975–1978.
Mazé, R. (1987), Generation and propagation of non-linear internal waves induced by tide over a continental slope, *Cont. Shelf Res.*, *7*, 1079–1104.
Mirshak, R., and D. E. Kelley (2009), Inferring propagation direction of nonlinear internal waves in a vertically sheared background flow, *J. Atmos. Oceanic Technol.*, *26*, 615–625.
Nash, J. D., S. M. Kelly, E. L. Shroyer, J. M. Moum, and T. F. Duda (2012), The unpredictable nature of internal tides on continental shelves, *J. Phys. Oceanogr.*, *42*, 1981–2000.
New, A. L. (1988), Internal tidal mixing in the Bay of Biscay, *Deep Sea Res., Part A*, *35*(5), 691–709.
New, A. L., and J. C. B. Da Silva (2002), Remote-sensing evidence for the local generation of internal soliton packets in the central Bay of Biscay, *Deep Sea Res., Part I*, *49*, 915–934.
New, A. L., and R. D. Pingree (2000), An inter comparison of internal solitary waves in the Bay of Biscay and resulting from Korteweg-de Vries-type theory, *Prog. Oceanogr.*, *45*, 1–38.
Pichon, A., and S. Correard (2006), Internal tides modeling in the Bay of Biscay. Comparisons with observations, *Sci. Mar.*, *70S1*, 68–88.
Pichon, A., and R. Mazé (1990), Internal tides over a shelf break: Analytical model and observations, *J. Phys. Oceanogr.*, *20*, 657–671.
Pichon, A., Y. Morel, R. Baraille, and L. S. Quaresma (2013), Internal tide interactions in the Bay of Biscay: Observations and modeling, *J. Mar. Syst.*, *109–110*, S26–S44, doi:10.1016/j.jmarsys.2011.07.003.
Pingree, R. D., and G. T. Mardell (1985), Solitary internal waves in the Celtic Sea, *Prog. Oceanogr.*, *14*, 431–441.
Pingree, R. D., and A. L. New (1989), Downward propagation of internal tidal energy into the Bay of Biscay, *Deep Sea Res., Part A*, *36*, 735–758.
Pingree, R. D., and A. L. New (1991), Abyssal penetration and bottom reflection of internal tidal energy in the Bay of Biscay, *J. Phys. Oceanogr.*, *21*, 28–39.
Pingree, R. D., G. T. Mardell, and A. L. New (1986), Propagation of internal tides from the upper slopes of the Bay of Biscay, *Nature*, *321*, 154–158.
Ramp, S. R., T. Y. Tang, T. F. Duda, J. F. Lynch, A. K. Liu, C.-S. Chiu, F. L. Bahr, H.-R. Kim, and Y.-J. Yang (2004), Internal solitons in the northeastern South China Sea Part I: Sources and deep water propagation, *IEEE J. Oceanic Eng.*, *29*, 1157–1181.
Scotti, A., R. C. Beardsley, and B. Butman (2007), Generation and propagation of nonlinear internal waves in Massachusetts Bay, *J. Geophys. Res.*, *112*, C10001, doi:10.1029/2007JC004313.
St. Laurent, L., and C. Garrett (2002), The role of internal tides in mixing the deep ocean, *J. Phys. Oceanogr.*, *32*, 2882–2899.
Xie, X. H., Y. Cuypers, P. Bouruet-Aubertot, B. Ferron, A. Pichon, A. Lourenço, and N. Cortes (2013), Large-amplitude internal tides, solitary waves, and turbulence in the central Bay of Biscay, *Geophys. Res. Lett.*, *40*, 2748–2754, doi:10.1002/grl.50533.